Infrared Physics and Technology 98 (2019) 27–35

Contents lists available at ScienceDirect

Infrared Physics & Technology

journal homepage: www.elsevier.com/locate/infrared

Regular article

Development of a low-cost microcomputer based vein imaging system

Mustafa Zahid Yildiz*, Ömer Faruk Boyraz

Department of Electrical & Electronics Engineering, Faculty of Technology, Sakarya University of Applied Sciences, 54187 Serdivan, Sakarya, Turkey

ARTICLE INFO

Keywords:
IR vein imaging system
Pixel based comparison
Raspberry Pi
Microcomputer

ABSTRACT

In this study, a low-cost microcomputer based dorsal hand-vein imaging system was developed by utilizing non-invasive near infrared imaging technology for the patients having hand vein visibility problems. On the microcomputer, we established a new database with high-quality dorsal-hand vein images. Pre- and post-processing were accomplished in Python language using Open-CV library on the microcomputer. Then, the specialist examined the whole obtained raw vein images to detect blood veins by marking the vein areas on a touch screen monitor, namely the reference images. The accuracy of the vein segmentation of our imaging system was assessed by comparing the reference images and the processed images on the microcomputer. We offered a novel simple pixel to pixel algorithm to test the segmented vein areas by the system. In addition, 2-D cross correlation algorithm was used for a secondary analysis. The average accuracy result of the 2-D cross correlation algorithms was 83.84% while pixel-based algorithm offered 94.47%. According to the results, we may conclude that the proposed vein imaging system do not produce suspicious unrelated vein areas which might create another clinical problem for the patients.

1. Introduction

Today, around 500 million daily vascular interventions take place in the world. According to the statistical information, even though about 95% interventions become successful at first attempt, around 14 million interventions become successful at second or successive trials. In order to solve out this important problem, a vascular imaging device might lead the process less painful for the patients, and will reduce the physical and mental burden of patients and health professionals. Thus, all other operations will be carried out on patients and performed more quickly in a healthy way. Difficulty of a vein cannulation depends on various factors such as blood volume, vein depth, the amount of adipose tissue, pigmentation. With these factors, to find vessels is almost impossible or quite difficult with the naked eye. The main reason for this is that the small size of the veins and lipid tissue [1]. One of the possible solutions of these kinds of problems is to improve the localization and visualization of blood vessels [2].

There are various techniques on vascular imaging. For instance, ultrasound is one of the methods used in vascular imaging, but it requires assistance, extra skills and costs high [3]. Another method of the vascular imaging is infrared light source to map vessel structures. In electromagnetic spectrum, between 740 nm and 1100 nm is called medical spectrum. In the vein imaging systems, the target area is illuminated by light sources at 700–1000 nm wavelength [4]. The light rays at these wavelengths penetrate the skin and absorbed by deoxygenated hemoglobin present in blood vessels more than other surrounding tissue. Thus, vein patterns appear darker with respect to the surrounding tissue on the captured images [5]. By utilizing the NIR imaging, there are many studies which use vein images for id matching [6–8] and authentication-based applications [9,10].

Far-infrared imaging (FIR) methods are extremely sensitive to environmental conditions and expensive. In contrast, near-infrared imaging methods are more tolerant to these conditions in both environment and body [11]. Thus, in the study, we used near infrared imaging modality. Most of the commercial vein imaging devices depend on galvanometric methods which have high spatial resolution [12]. Because of their high expenses, these systems cannot be commonly used in many hospitals. On the other hand, many cheaper solutions have very low image resolution and signal to noise ratio. In order to increase the image contrast, there are successful methods in the literature such as Retinex theory, histogram equalization, contrast limited adaptive histogram equalization (CLAHE) [13,14], median and Gaussian filtering [15,16]. Unfortunately, in contrast enhancement methods based on histogram equalization, some of the vein patters disappear thereby losing some important data. In our current study, to prevent the detail information loss, we applied CLAHE method.

In the study by Shrotri et al. [17], hand palm images were recorded by a webcam (Logitec Pro 2000) and they used a 760 nm led array for

* Corresponding author.
E-mail address: mustafayildiz@sakarya.edu.tr (M.Z. Yildiz).

https://doi.org/10.1016/j.infrared.2019.02.010
Received 22 December 2018; Received in revised form 15 February 2019; Accepted 16 February 2019
Available online 18 February 2019
1350-4495/

illumination. They developed a personal computer-based vein imaging system. They claimed that all the system cost around 25 USD. The image processing algorithms was developed by OpenCV libraries. The contrast of the images was arranged by controlling the power supply output of the led system. Even though the system was affordable for many hospitals and end users, all system depends on the personal computer performances. As a disadvantage of their system, the resolution of the system was quite low, which is one the most crucial of the imaging systems. In the study by Wang et al., FIR and NIR imaging methods were compared. They showed that NIR imaging produced high resolution and low noise images and was cheaper than FIR systems [18]. They claimed that FIR systems are more vulnerable to outside conditions such as temperature and humidity. One of the most challenging problems in NIR imaging was the hairs and scars on the skin surfaces [19]. In an experimental study by Lin and Fan, a thermal camera-based vein imaging system was used. They produced a vein image database and developed an ID recognition system based on image comparison. Their system cost about 8000 USD which is again not an affordable amount for many clinics in the world [20]. Crisan et al. developed another system based on NIR imaging. They used a 720 nm light source and NIR filter around 720 nm cut off frequency. Even though the system was cheaper, the main disadvantage of their system was the immobility [21]. In an important study by Gayathri et al., a Linux operational system-based hand vein ID recognition system was developed. There was CCD camera and 24 IR led arrays. They selected a triangle targeted area and used histogram equalization procedures. After application of some morphological procedures, they used cross-correlation method for ID recognition. The main disadvantage of the system was the results was not quantified and supported by a statistical test [22].

In this current study, the main objective was to develop a mobile IR vein imaging system which capable of segmenting the dorsal hand vein of human subjects on a cheap microcomputer in near real-time. In many vein imaging system, back-projection of the segmented vein region is very crucial before the injection or any vein related invasive applications. Many vein imaging systems use only contrast enhancement methods and projects back to the target area. We accomplished all the image registration, preprocessing and morphological methods on the Raspberry Pi 3. In addition, unlike many studies focusing on id matching, our primary goal was to assess the efficiency of the system by a simple method. Thus, we offer a simple novel pixel-based comparison method to find real vein areas in accordance with the reference vein image database marked by a specialist. In addition, we tried a second validation by 2-D cross correlation for further analysis. The experimental results show that our imaging system is capable enough to present dorsal vein images and might be a good candidate for id matching and biometric authentication systems.

2. Materials and Methods

2.1. Participants

72 healthy adults (40 males, 32 females, age range: 18–35) participated in the study (P1-P72). None of them had any vein surgery or other medical condition which could have affected the results presented here. Subjects were asked to place their right and left hands at fist position under the infrared camera on a white surface during 10 s. The procedures posed no harm for the participants. All participants gave written consents and the experiments were approved by the Institutional Review Board for Research with Human Subjects of Sakarya University (no.71522473/050.01.04/86). Because of the sensitivity of the ambient light conditions, all the experiments were conducted in the Biomedical Instrumentation Laboratory, Sakarya University.

2.2. Materials

By utilizing the absorption property of the hemoglobin in red blood cells of infrared rays, blood vessels are allowed to be displayed differently from other tissues. According to studies in the literature, the vein regions appear darker with respect to the surrounding tissue at 850 nm infrared wavelength [23]. The absorption of deoxyhemoglobin has a peak value close to 750 nm. However, the maximum intensity ratio between the blood vessel and the surrounding tissue has a peak value close to 850 nm [24]. In the vein visualities process, the advantage of the maximum density ratio is much better than the disadvantage of deoxyhemoglobin absorption (in 850 nm).

Due to the fact that the vein regions were seen better at this wavelength, leds with wavelength of 850 nm were used. In this study, with the help of this absorption property, two 850 nm 1 W near-infrared (NIR) power Light Emitting Diode (LED, Edison-Opto, Taiwan) were used to illuminate the hand surfaces of the voluntary subjects. Two high power 1 W infrared LEDs were focused on the target area and mounted to the left and right of the camera. The camera and LEDs were connected to the Raspberry Pi with flex cable. The Raspberry Pi and NIR LEDs were derived by a 5 V 2.5-A power supply. The illumination was almost constant during the experiment with the help of constant current supply of the LED system.

In order to record the reflected lights from the subject, an RGB-Infrared camera module of the Raspberry Pi 3 (Galler, Raspberry Pi Foundation) was used.

The size of the infrared camera card is approximately 25 mm × 24 mm × 9 mm. Size and weight are an important parameter for mobile or other applications. Therefore, having a weight of just over 3 gr provides a positive advantage. It connects to Raspberry Pi by way of a short ribbon cable. The camera is connected to the BCM2835 processor on the Pi via the CSI bus. This is a higher bandwidth link that transmissions the pixel data from the camera back to the processor. This bus travels along the ribbon cable that attaches the camera board to the Raspberry Pi. The sensor has a resolution of 5 Megapixels (Omnivision 5647) and has a fixed focus lens onboard [25]. In terms of still images, the camera is capable of 2592 × 1944-pixel static images, and also supports 1080p30 (30 frames per second), 720p60 and 640 × 480p60/90 video.

An optical narrow band pass filter (Kodak 87C Wratten) was attached to the camera module in order to eliminate the visible lights and increase the signal to noise ratio. After recording the raw images, various signal processing methods were applied which were shown at following method sections. The data was processed by a portable Raspberry Pi 3 microcomputer. The processed data was visualized by a 7-inch touch screen module via HDMI connection. The general block diagram of the whole system was shown at Fig. 2.1. All the data recording and processing was near real-time.

2.3. Methods

After capturing the raw image from the IR camera module, an open source Open-CV image processing library was used in Phyton programming language. Hence, the vein patterns were detected by gray scale conversion, contrast limited adaptive histogram equalization, median filtering, adaptive thresholding, binarization and morphological operations (opening, closing and erosion) respectively. All the process was shown on the block diagram, Fig. 2.2

2.3.1. Gray scale conversion

To convert colored image in to grayscale, the weighted mean values of red, green and blue are calculated. Grayscale weighted mean value was calculated with the equation given below. In the Eq. (1); r, g and b are color values that can be taken integer value between 0 and 255.

$$x = (0.299 \times r) + (0.587 \times g) + (0.114 \times b) \quad (1)$$

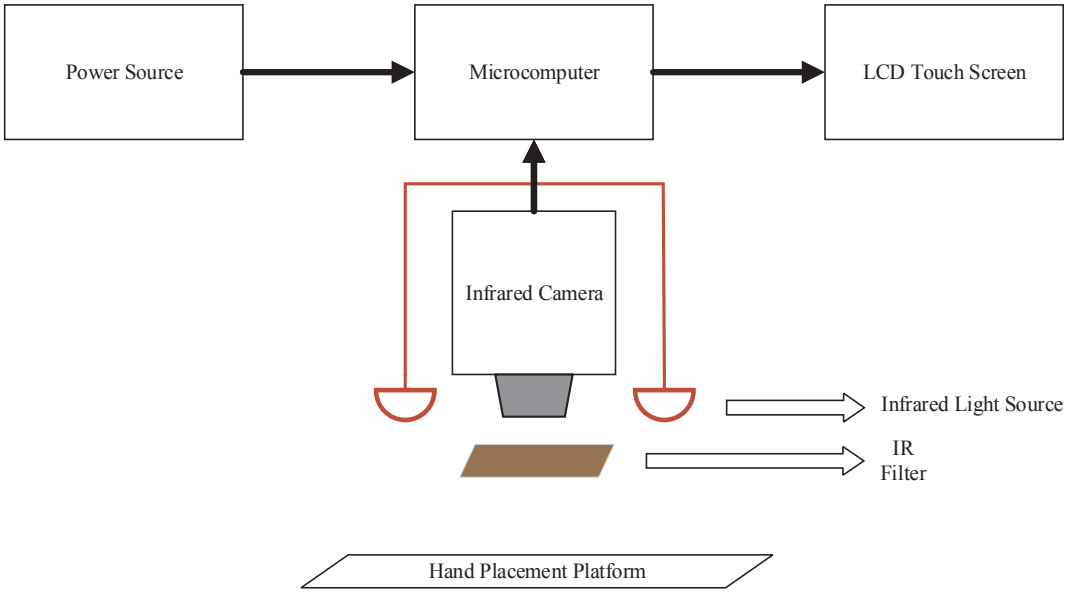

Fig. 2.1. Block diagram of the hardware system.

As it can be seen in the equation above the coefficient of the colors are not equal. The reason for this the raw green is lighter color than the raw red and the raw blue, thus green color has bigger coefficient. The raw blue is the darkest one out of the three color to the human eye; thus, the raw blue has the lowest coefficient [26].

2.3.2. Contrast limited adaptive histogram equalization (CLAHE)

CLAHE is a technique to increase the regional contrast in an image [27]. In the medical imaging systems, the technique is proved useful for enhancing low contrast images [28–30].

In this approach, the histogram of each region is calculated as a first step. Then, the clipping threshold value is obtained according to desired contrast window width. In the next step, each histogram value is re-assigned without exceeding the pre-determined threshold value. In the final step, the cumulative distribution function (CDF) of the histograms is determined for grayscale mapping. In CLAHE method, pixels are mapped with their closest four neighbors. The bottom regions are merged with bi-linear interpolation. The regions are divided into three groups named IR (inner Region), CR (corner region) and BR (border region) according to their neighboring conditions as it can be seen in Fig. 2.3.

The first group consists of four corner regions (CR), the second group consists of twenty-four border regions (BR). Except for the corner regions, all the regions in the image border belongs to this class. The last group consists of thirty-six regions which remains inner parts are called inner region (IR).

Each region consists of four quarters. In this way, as it can be seen in Fig. 2.4 each quarter in every region in IR group has four neighbors.

In this situation, the new values of the pixels in IR region is calculated with the equation given below:

$$\rho_{new} = \frac{s}{r+s} \times \left(\frac{y}{x+y} \times f_{i-1,j-1}(\rho_{old}) + \frac{x}{x+y} \times f_{i,j-1}(\rho_{old}) \right) + \frac{r}{r+s} \times \left(\frac{y}{x+y} \times f_{i-1,j}(\rho_{old}) + \frac{x}{x+y} \times f_{i,j}(\rho_{old}) \right) \quad (2)$$

The neighborhood structure for the region in BR group is little different. The neighborhood structure of the pixels in the first and the third quarters in the rightmost regions and the second and fourth quarters in the leftmost regions are same as that of in IR group regions. However, the pixels values in the second and fourth quarters in the rightmost regions and the first and the third quarters in the leftmost regions are calculated as follows:

$$\rho_{new} = \frac{s}{r+s} \times f_{i,j-1}(\rho_{old}) + \frac{r}{r+s} \times f_{i,j}(\rho_{old}) \quad (3)$$

For the regions in CR group, the different quarters have different characteristic properties. The first quarter in this group has different condition than the other ones. The reason for this, the first quarter has non-neighboring pixels. However, the pixels in the fourth quarter have neighborhood structure like in IR group regions, the pixels in the second and the third quarters have neighborhood structure like two side quarters in BR regions. In the top-left corner of Fig. 2.5, CR group region and its neighborhood is shown.

The values of non-neighboring pixels in the first quarter remain

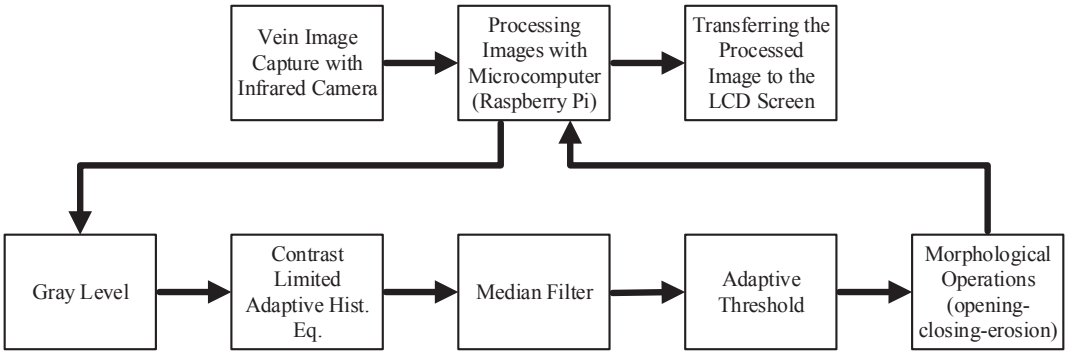

Fig. 2.2. Block diagram of the software system.

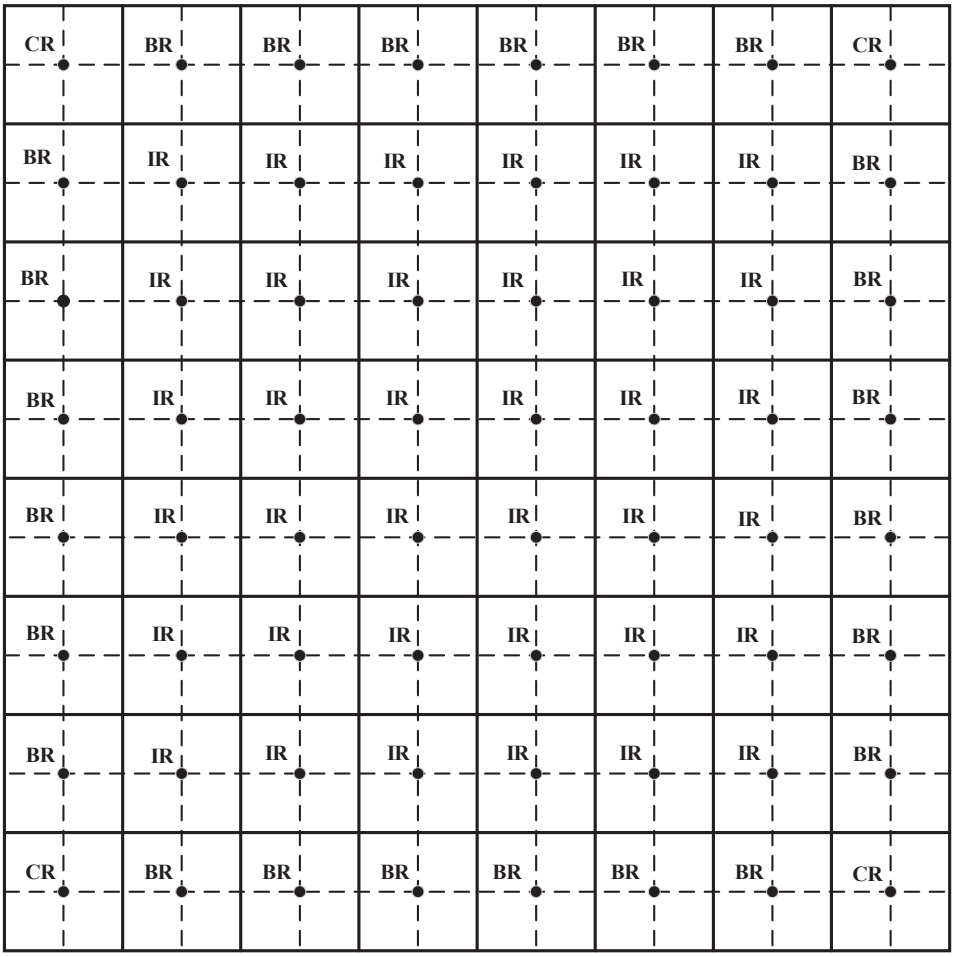

Fig. 2.3. An example of 512 × 512 image divided into 64 identical squares [31].

unchanged:

$$\rho_{new} = f_{i,j}(\rho_{old}) \tag{4}$$

In this way, for each region the result image is obtained by doing grayscale mapping. This method is used on medical images to both reduce noise and to remove the effects of side shadow in the homogeneous regions [32].

2.3.3. Median filter

As it can be understood from its name, in the median filter a pixel value is changed with its median value of the mean values in its neighborhood region.

To apply median filter operation on a point in an image, the gray tones in the mask are arranged according to their pixel values. Then, the median value is found and this value is assigned to the corresponding pixel in the filtered image. This operation is stated as follow:

$$G(i,j) = Median\{F_1(i,j), F_2(i,j), \ldots\ldots\ldots, F_n(i,j)\} \tag{5}$$

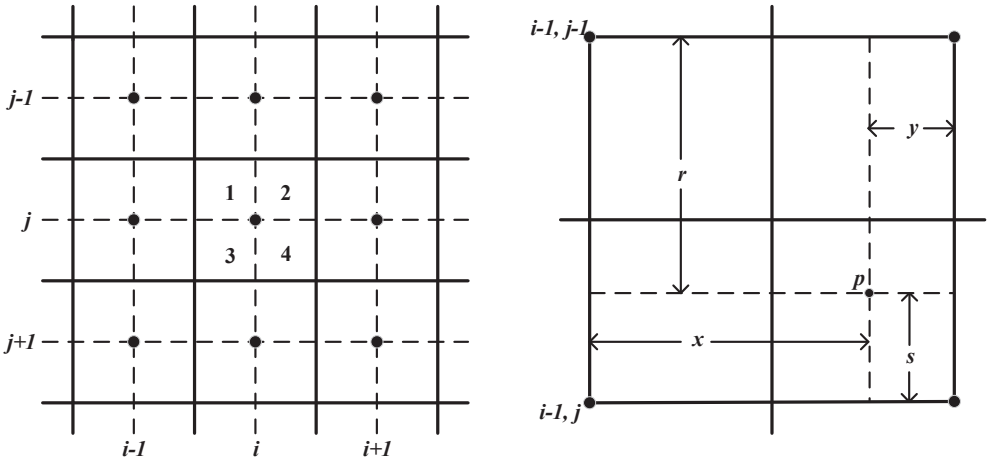

Fig. 2.4. a. A given IR region with its all neighboring regions. b. The first quarter of *(i,j)* region and its relations with the closest four regions [31].

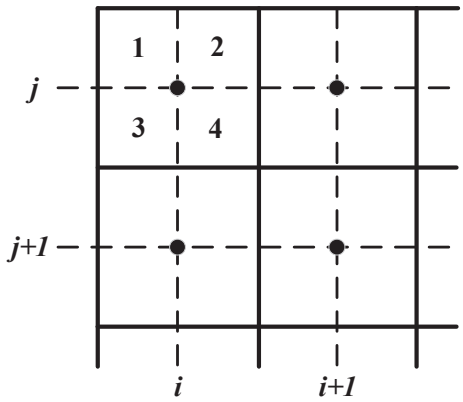

Fig. 2.5. CR region in the top-left corner and its neighborhood structure [31].

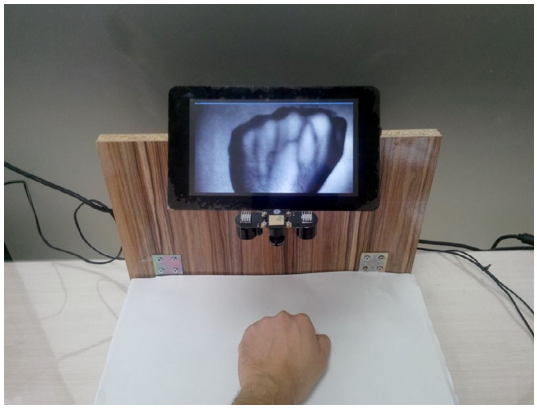

Fig. 2.6. Data acquisition procedure of the vein-pattern imaging system.

The median filter, a non-linear low pass filter, is used to reduce salt-pepper, speckle and impulsive noises [33].

2.3.4. Local thresholding

Local thresholding employs standard deviation and mean value of each neighboring pixel of all points in an image. This two values are very useful for calculating local thresholding since they define contrast and mean intensity. σ_{xy} and m_{xy} in an image show standard deviation and mean values respectively for pixel clusters in the neighborhood of T_{xy} that is centered at (x,y) coordinates. Local thresholding variables are stated commonly as follow:

$$T_{xy} = a \times \sigma_{xy} + b \times m_{xy} \tag{6}$$

In the Eq. (6), a and b are non-negative constants. For an image in the neighborhood of T_{xy} the standard deviation and mean values are given below respectively:

$$\sigma_{xy} = \sqrt{\frac{1}{M \times N} \times \left(\sum_{x=0}^{M-1} \sum_{y=0}^{N-1} [f(x,y) - m]^2 \right)} \tag{7}$$

$$m_{xy} = \frac{1}{M \times N} \times \left(\sum_{x=0}^{M-1} \sum_{y=0}^{N-1} f(x,y) \right) \tag{8}$$

If the standard deviation and the mean values calculated with the equations above are put in the Eq. (6) the threshold value which is in the neighborhood of T_{xy} is determined. Then, the segmented image in the local thresholding is defined as follow:

$$g(x,y) = \begin{cases} 1 & if \quad f(x,y) > T_{xy} \\ 0 & if \quad f(x,y) \leqslant T_{xy} \end{cases} \tag{9}$$

2.3.5. Morphological operations

In biology, morphology is about form and structure of living organism. The mathematical morphology is based on basic cluster operations to define and extract structures like borders and skeletons in image and it is a necessary tool for segmentation and removing noise.

In the opening operation objects and the gap between objects in the image are removed according to the size of the structuring element. The objects in the image get smaller than their pattern in the original image. With the opening operation, the two close objects in the image get separated without causing much change in the image [34]. The opening operation is a useful method to remove noises in the image.

Binary opening operation is defined as:

$$A \circ B = (A \Theta B) \oplus B \tag{10}$$

After the closing operation, dots (points) in the image closes each other and baseline in the image gets enlarged. Like in the dilation operation, the gaps between closer points are filled and the points are merged. The objects remain in the image form patterns as in the original image. Binary closing operation is defined as:

$$A \bullet B = (A \oplus B) \Theta B \tag{11}$$

The closing operator is a method to remove small holes or black dots of the objects in foreground region of the image [35].

Erosion is a morphologic operator that is used for thinning or shrinking objects in the binary image. The effect of the operator is eroding the image from its edges. The operator shrinks the size of objects in a binary image according to the chosen structuring element. Objects in image get smaller, the holes get expand if there any and the linked objects have tendency to separate.

For given "A: processed image" and "B: structuring element" clusters in Z^2 universe, the erosion operation is defined as:

$$A \Theta B = \{ z \mid (B)_z \subseteq A \} \tag{12}$$

The structuring element created in this operation from zeros and ones is moved pixel by pixel. If the center pixel of the filter encounters with value "1″ the situation of the pixels in the filter is investigated. If there is any "0" valued pixel in the picture that is underneath the filter's "1" valued pixel, all pixels which are underneath filter's "1" valued pixels are changed to "0".

2.3.6. Data acquisition and experimental procedures

In this study, in order to acquire the vein images, NIR imaging technology was used. Left and right surface of the hands of the subjects were illuminated by two 850 nm IR power leds. A narrow band Kodak written filter (cut off frequency: 850 nm) was attached to mini Raspberry Pi IR camera. By the IR filter, the effect of visible light and oscillating light conditions were eliminated. The illumination was almost constant during the experiment with the help of constant current supply of the LED system (Fig. 2.6).

The subjects were asked to place their hand as illustrated on the Fig. 2.6. There was a marker on the surface for correct positioning. The number of subjects was explained on the participants section above.

2.3.7. Analysis

The most important part of the study was the statistical evaluation of the ID recognition result. All the vein patterns were validated and inspected by a medical doctor at Sakarya University Medical School. The regions of interest were selected by the same doctor. Later, adaptive thresholding was applied on the vein pattern selected by specialist. The selected area of the vein pattern was processed by the microcomputer and the accuracy of two different methods were compared, namely, 2-D cross correlation and pixel-based comparison. The results were statistically tested by the Shapiro Wilk normalization analysis [36]. If the data was normally distributed, a parametrical t-test was used to detect any statistical difference.

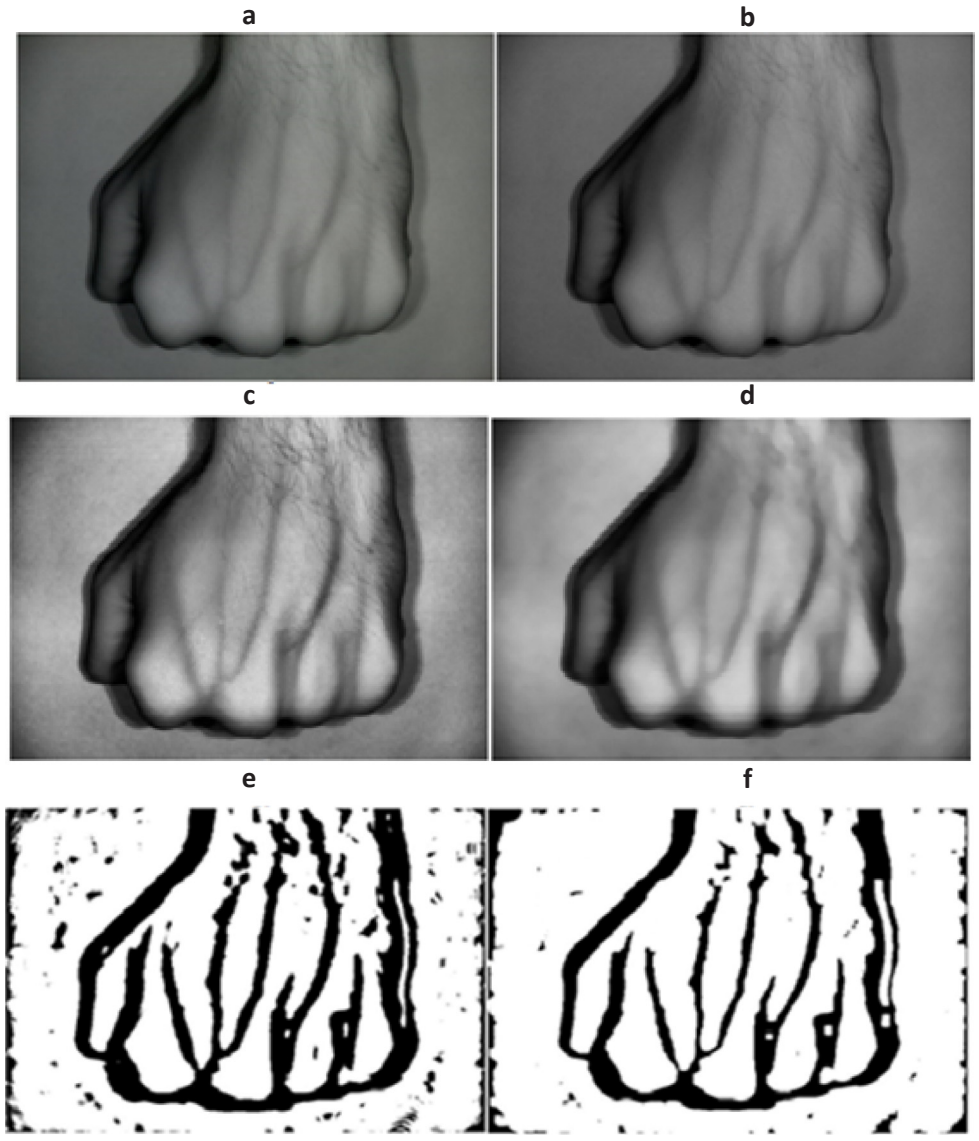

Fig. 3.1. (a) Raw image (b) Gray scale image (c) Contrast limited adaptive histogram equalization (d) Median filtering (e) Adaptive thresholding (f) Opening, closing, erosion. (Subject #27).

2.3.7.1. 2-D cross correlation. The correlation coefficients will have the values between $-1 \leq r \leq 1$ showing positive or negative correlation of the data. When the value *"r"* is close to 0, the correlation between the variables is said to be weak [37]. We used following correlation formula and run the algorithm on the Raspberry Pi 3 microcomputer. In the Eq. (13), A corresponds to reference, and B is the test images.

$$r = \frac{\sum_{i=1}^{M}\sum_{j=1}^{N}(A_{i,j} - \bar{A})x(B_{i,j} - \bar{B})}{\sqrt{\left(\sum_{i=1}^{M}\sum_{j=1}^{N}(A_{i,j} - \bar{A})^2\right)x\left(\sum_{i=1}^{M}\sum_{j=1}^{N}(B_{i,j} - \bar{B})^2\right)}} \quad (13)$$

2.3.7.2. Pixel-based comparison. We propose a new simple method in vein pattern matching systems. In this method, the target area selected by a medical specialist was tested after the image processing applications. Based on this method, the percentage of overlapping patterns were calculated. The pixel-based comparison method has the following steps;

$$Matching\_percentages = 100x\frac{Matching\_black\_pixel}{Matching\_black\_pixel + Unmatched\_pixel} \quad (14)$$

(1) The image of target area is recorded.
(2) 8-bit images are converted to 1-bit, and "integer" values are converted to "double".
(3) The size of the images are calculated.
(4) The number of different between reference image and target image is calculated. These results show the non-vein area of the image.
(5) The matching (black) pixels are calculated.
(6) The matching pixels are divided to total number of pixels.
(7) The resulting value is multiplied by 100 to find out overlapping the percentage.

3. Results

In this section, the raw hand image data captured by IR camera are presented. The raw data is processed and send to the specialist. All image processing steps were explained in the method section above.

The raw image captured by IR camera is converted to 8-bit 256 Gy scale level. The raw and gray scale images are shown on the Fig. 3.1a and b. At second step, the gray scale image is exposed to contrast limited histogram equalization (CLAHE). Thus, the vein patterns appear darker on the hand surface (Fig. 3.1c).

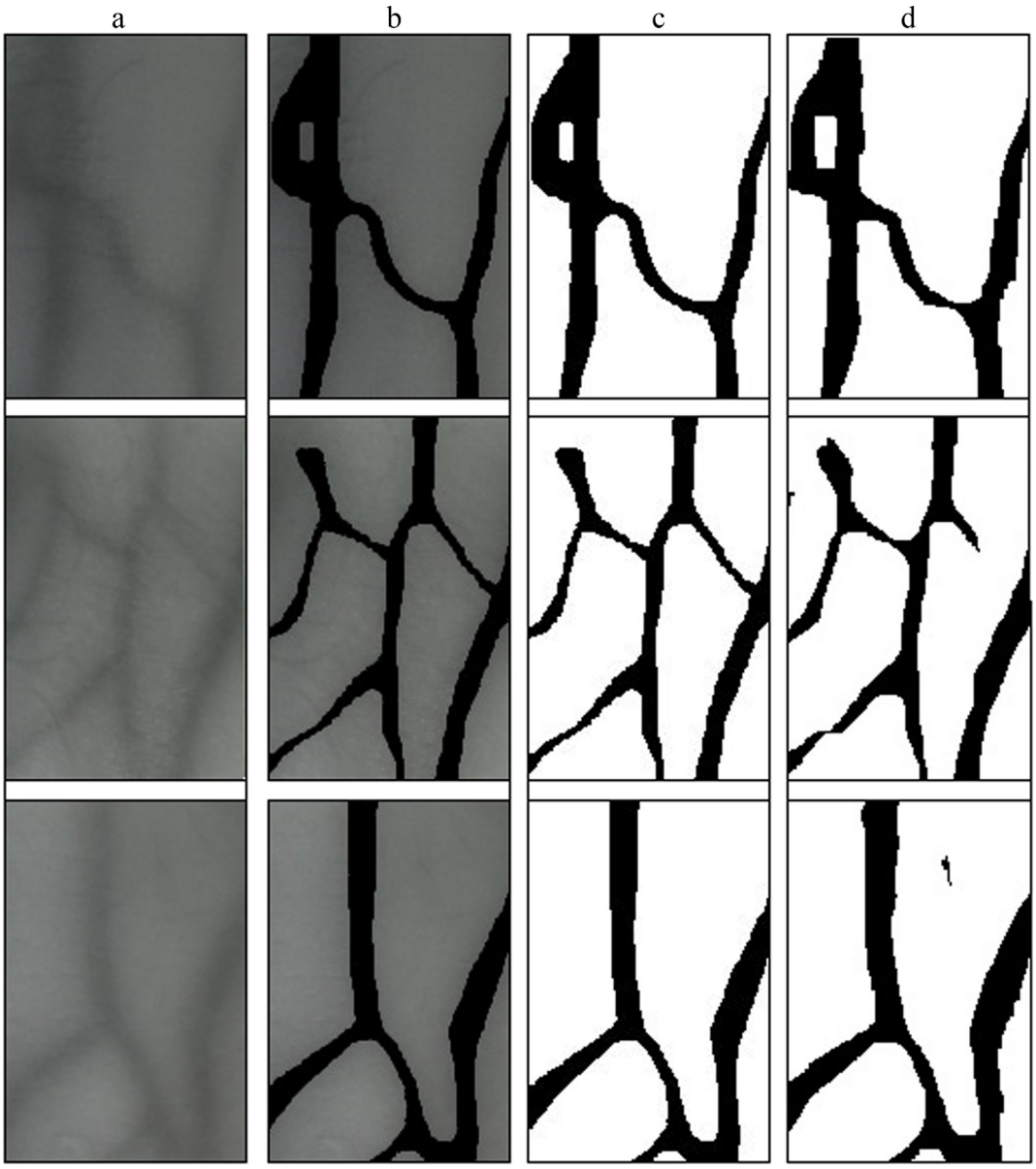

Fig. 3.2. (a) 120 × 180 raw data (b) Reference image by the medical doctor c) Binary conversion of selected area d) after all image processing steps.

Table 3.1
Accuracy of vein pattern recognition for selected 120 × 180 pixel area for 2-D cross correlation and pixel-based comparison.

No	Two-dimensional cross correlation (%)	Pixel-based comparison (%)
Mean	83.84	94.47
Std	4.19	2.6
Min	75.33	89.01
Max	90.94	98.57

After contrast limited histogram equalization, a 5 × 5 pixels window median filtering is applied. The purpose of this filter is to eliminate hairs and wrinkles on the skin. On the Fig. 3.1d, because of the effect of median filtering, the hairs of the skin were eliminated. After this partly noise removal process, the vein pattern is segmented from the background. From this point, the image is converted to 1 bit (0–255) from 8 bit. After the median filtering, the result of the thresholding is shown in Fig. 3.1e.

On the last step, three morphological process were applied, namely, opening, closing and erosion. These steps are explained in the method section above. After the morphological process (Fig. 3.1f), the data is sent to the specialist to verify and select the target area for statistical comparison.

3.1. Matching pixel percentage detection

From the Fig. 3.1f, a triangular120x180 pixel was selected as a region of interest. From this area, a two-dimensional cross correlation and a simple pixel-based comparison algorithm were computed. In Fig. 3.2, there are three different examples of vein patterns from the randomly selected subjects.

From the 72 captured images, all images are selected by the medical doctor. This specialist selected target area and created reference images. By using these reference images, two different methods were tested for vein pattern accuracy. The comparison results are given in the Table 3.1.

In Fig. 3.2.a the raw data from three subjects hand surfaces were shown. In Fig. 3.2b the vein images are selected by the specialist according to his experience. In Fig. 3.2c, the picture is converted to the binary scale. At last, in Fig. 3.2d all the image processing algorithms

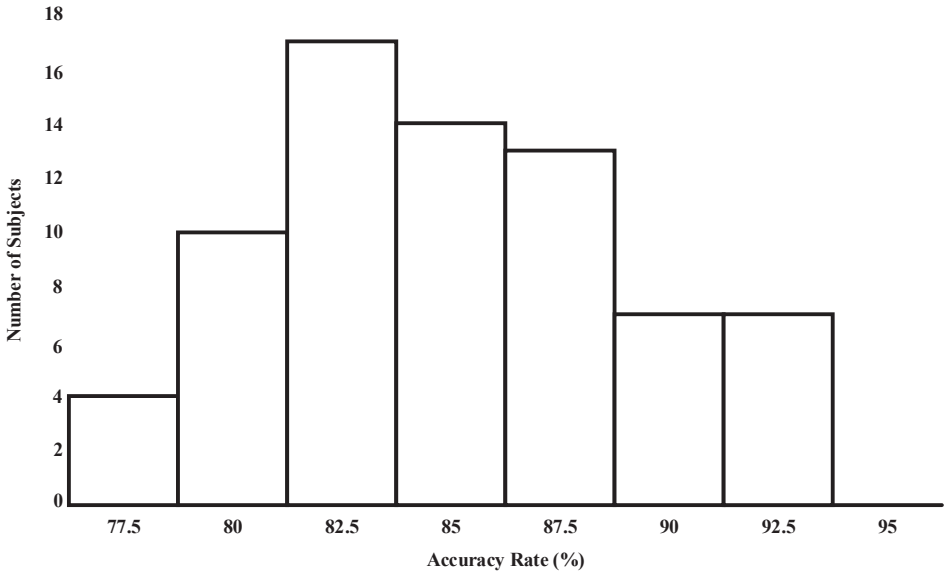

Fig. 3.3. Histogram of 2-D cross correlation accuracy results.

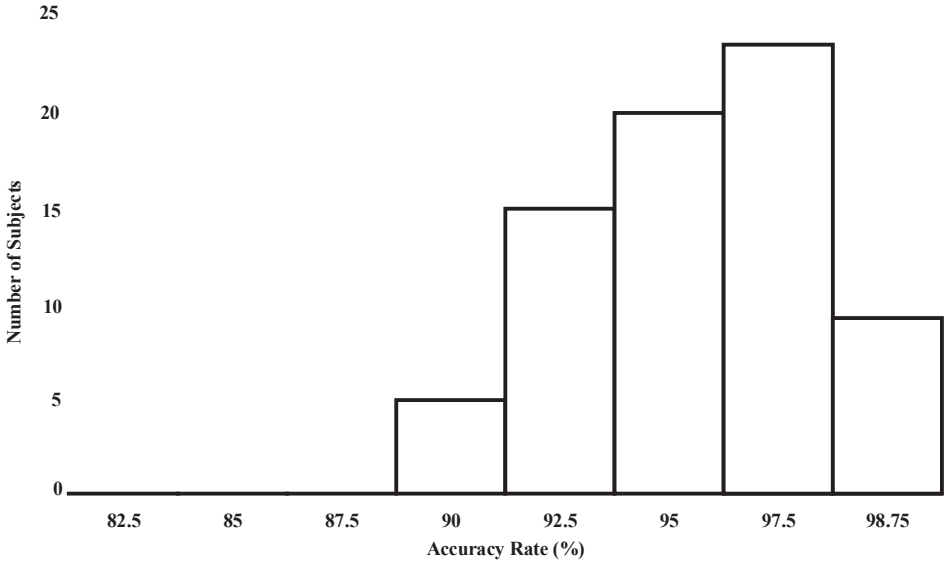

Fig. 3.4. Histogram of the pixel based comparison results.

Table 3.2
Summary of accuracy values of the two indicated methods.

	Number of data	Average	Standard Deviation	Mean Standard Error
Two-dim. cross correlation	72	83.84	4.19	0.49
Pixel-based comparison	72	94.47	2.6	0.31

were applied, which were explained above in method sections.

As for comparison results, two-dimensional cross correlation and pixel-based comparisons percentages were tabulated for the subjects (Table 1). It was shown that the maximum pattern recognition accuracy value was 90.94% in 2-D correlation, where as it was maximum 98.57%.

Before the statistical comparison of these accuracy values, a Shapiro Wilk normality test was used. The histogram of the 2-D cross correlation result is shown in the Fig. 3.3. The average accuracy was found 83.84% with a standard deviation 4.19. The normality test significance level was p = 0.994 showing the data is normally distributed. In the pixel-based comparison algorithm, average accuracy was found 94.47% with a standard deviation 2.6. The normality test showed statistical significance ($p = 0.61$) indicated that the data was normally distributed. The histogram of the pixel-based comparison result is shown in the Fig. 3.4.

In Table 3.2, the summary of accuracy percentage values for 2-D cross correlation and pixel-based comparison methods were given.

According to the paired *t*-test, the accuracy of pixel-based comparison showed statistically significant performance ($p = 0.000117$, $p < 0.05$) than the 2-D cross correlation method.

4. Conclusion

In the vein imaging technologies, there are different approaches based on software and hardware. In the literature, scientist have developed FIR and NIR vein image devices and complex algorithms. There are also commercialized devices suitable for clinical use. The main disadvantage of the previous systems, they are mostly not mobile and they do not show statistical accuracy of vein pattern matching. Their prices are also quite high, which is not affordable for many of the hospitals or clinics. The main purpose of this study was to overcome the mobility problems and decrease the cost of the system.

In this study, the hardware system cost approximately 75 US Dollars. The software was open source and free of charge. One of the main advantages of the system was that all the image processing was accomplished online on the microcomputer. Additionally, vein database was established without requiring an additional PC.

After preprocessing and morphological operations were used for vein segmentation. We used two algorithms to check the real vein areas on the recorded database. The reference images from the specialist were compared based on 2-D cross correlation and a novel simple pixel based comparison methods. The parametric paired *t*-test was applied on 72 vein patterns. The result showed that pixel based algorithm showed statistically significant performance on pattern extraction.

All in all, the presented low cost NIR vein imaging system might be a good candidate for ID recognition and biometric authentication systems. In the future, we plan to acquire more hand vein data and update the software for biometric purposes.

Conflict of interest

The authors have declared no conflict of interest

Acknowledgement

This study was supported by TUBITAK funding no. 118E235 to Assist. Prof. Dr. Mustafa Zahid YILDIZ. The authors thank Dr. Dogan ERDOGDU for evaluating vein images manually and suggestions in the initial design of the experiments, and for critical comments on the paper. The authors are grateful to Biomedical Instrumentation Lab. Students for their contributions and being volunteers for the experiments. This study was accepted by Sakarya University Research Ethics Committee (no. 71522473/050.01.04/86).

References

[1] N.J. Natascha, J.C. Graaff, R.M. Verdaasdonk, C.J. Kalkman, Near-infrared imaging in intravenous cannulation in children: a cluster randomized clinical trial, Pediatrics 131 (2013), https://doi.org/10.1542/peds.2012-0968d.
[2] N.J. Cuper, J.H. Klaessens, J.E. Jaspers, R.D. Roode, H.J. Noordmans, J.C.D. Graaff, et al., The use of near-infrared light for safe and effective visualization of subsurface blood vessels to facilitate blood withdrawal in children, Med. Eng. Phys. 35 (2013) 433–440, https://doi.org/10.1016/j.medengphy.2012.06.007.
[3] S.J. Doniger, P. Ishimine, J.C. Fox, J.T. Kanegaye, Randomized controlled trial of ultrasound-guided peripheral intravenous catheter placement versus traditional techniques in difficult-access pediatric patients, Pediatr. Emerg. Care 25 (2009) 154–159, https://doi.org/10.1097/pec.0b013e31819a8946.
[4] Q. Zhu, Z. Zhang, N. Liu, H. Sun, Near infrared hand vein image acquisition and ROI extraction algorithm, Optik. 126 (2015) 5682–5687, https://doi.org/10.1016/j.ijleo.2015.09.001.
[5] F. Wang, A. Behrooz, M. Morris, A. Adibi, High-contrast subcutaneous vein detection and localization using multispectral imaging, J. Biomed. Opt. 18 (2013) 050504, https://doi.org/10.1117/1.jbo.18.5.050504.
[6] S. Barra, M.D. Marsico, M. Nappi, F. Narducci, D. Riccio, A hand-based biometric system in visible light for mobile environments, Inf. Sci. 479 (2019) 472–485, https://doi.org/10.1016/j.ins.2018.01.010.
[7] D. Huang, R. Zhang, Y. Yin, Y. Wang, Y. Wang, Local feature approach to dorsal hand vein recognition by centroid-based circular key-point grid and fine-grained matching, Image Vis. Comput. 58 (2017) 266–277, https://doi.org/10.1016/j.imavis.2016.07.001.
[8] D. Huang, X. Zhu, Y. Wang, D. Zhang, Dorsal hand vein recognition via hierarchical combination of texture and shape clues, Neurocomputing 214 (2016) 815–828, https://doi.org/10.1016/j.neucom.2016.06.057.
[9] J. Wang, G. Wang, Hand-dorsa vein recognition with structure growing guided CNN, Optik 149 (2017) 469–477, https://doi.org/10.1016/j.ijleo.2017.09.064.
[10] J. Wang, G. Wang, M. Li, W. Du, Hand vein recognition based on PCET, Optik 127 (2016) 7663–7669, https://doi.org/10.1016/j.ijleo.2016.05.119.
[11] E.C. Lee, H. Jung, D. Kim, New finger biometric method using near infrared imaging, Sensors 11 (2011) 2319–2333, https://doi.org/10.3390/s110302319.
[12] G. Dan, Z. Guo, H. Ding, Y. Zhou, Enhancement of dorsal hand vein image with a low-cost binocular vein viewer system, J. Med. Imaging Health Informat. 5 (2015) 359–365, https://doi.org/10.1166/jmihi.2015.1400.
[13] H.S. Cha, S.H. Hong, Advanced retinex algorithm for image enhancement, J. Korea Multimedia Soc. 16 (2013) 29–41, https://doi.org/10.9717/kmms.2013.16.1.029.
[14] M. Yakno, J.M. Saleh, B.A. Rosdi, Low contrast hand vein image enhancement, 2011 IEEE International Conference on Signal and Image Processing Applications (ICSIPA), 2011, https://doi.org/10.1109/icsipa.2011.6144135.
[15] C.L. Lin, An approach to improve the quality of infrared images of vein-patterns, Sensors 11 (2011) 11447–11463, https://doi.org/10.3390/s111211447.
[16] L. You, L. Sun, F. Li, X. Li, Finger Vein Recognition Method Based on Gaussian Low-Pass Filter and Direction Detection, 2014 International Conference on Information and Communications Technologies (ICT 2014), 2014, https://doi.org/10.1049/cp.2014.0598.
[17] D. Bhattacharyya, A. Shrotri, S.C. Rethrekar, M.H. Patil, F.A. Alisherov, T.H. Kim, Biometric Authentication Using Infrared Imaging of Hand Vein Patterns, Communications in Computer and Information Science Information Security and Assurance, 2010, pp. 108–115, , https://doi.org/10.1007/978-3-642-13365-7_11.
[18] L. Wang, G. Leedham, S.Y. Cho, Infrared imaging of hand vein patterns for biometric purposes, IET Comput. Vision 1 (2007) 113–122, https://doi.org/10.1049/iet-cvi:20070009.
[19] A. Shahzad, N. Walter, A.S. Malik, N.M. Saad, F. Meriaudeau, Multispectral venous images analysis for optimum illumination, selection, 2013 IEEE International Conference on Image Processing, 2013, https://doi.org/10.1109/icip.2013.6738491.
[20] C.L. Lin, K.C. Fan, Biometric verification using thermal images of palm-dorsa vein patterns, IEEE Trans. Circuits Syst. Video Technol. 14 (2004) 199–213, https://doi.org/10.1109/tcsvt.2003.821975.
[21] S. Crisan, J.G. Tarnovan, T.E. Crisan, A low cost vein detection system using near infrared Radiation, 2007 IEEE Sensors Applications Symposium, 2007, https://doi.org/10.1109/sas.2007.374359.
[22] S. Gayathri, K.G.J. Nigel, S. Prabakar, Low cost hand vein authentication system on embedded linux platform, Int. J. Innovative Technol. Exploring Eng. 2 (2013) 138–141.
[23] D. Ai, J. Yang, J. Fan, Y. Zhao, X. Song, J. Shen, et al., Augmented reality based real-time subcutaneous vein imaging system, Biomed. Opt. Exp. 7 (2016) 2565, https://doi.org/10.1364/boe.7.002565.
[24] B. D'Alessandro, A.P. Dhawan, Transillumination imaging for blood oxygen saturation estimation of skin lesions, IEEE Trans. Biomed. Eng. 59 (2012) 2660–2667, https://doi.org/10.1109/tbme.2012.2209647.
[25] Raspberry Pi Camera Board - Night Vision & Adjustable-Focus Lens (5MP), MODMYPI LTD, (accessed February 14, 2019), < https://www.modmypi.com/raspberry-pi/camera/camera-boards/raspberry-pi-night-vision-camera > .
[26] C. Saravanan, Color Image to Grayscale Image Conversion, 2010 Second International Conference on Computer Engineering and Applications, 2010, https://doi.org/10.1109/iccea.2010.192.
[27] K. Zuiderveld, Contrast limited adaptive histogram equalization, Graphics Gems. (1994) 474–485, https://doi.org/10.1016/b978-0-12-336156-1.50061-6.
[28] A.M. Reza, Realization of the contrast limited adaptive histogram equalization (CLAHE) for real-time image enhancement, J. VLSI Signal Process.-Syst. Signal, Image, Video Technol. 38 (2004) 35–44, https://doi.org/10.1023/b:vlsi.0000028532.53893.82.
[29] L. Li, Y. Si, Z. Jia, Medical image enhancement based on CLAHE and unsharp masking in NSCT domain, J. Med. Imaging Health Informat. 8 (2018) 431–438, https://doi.org/10.1166/jmihi.2018.2328.
[30] S. Gupta, S. Singh, Curvelet based Rayleigh CLAHE Medical Image Enhancement, Int. J. Comput. Appl. 182 (2018) 19–23, https://doi.org/10.5120/ijca2018917554.
[31] Z. Al-Ameen, G. Sulong, A. Rehman, A. Al-Dhelaan, T. Saba, M. Al-Rodhaan, An innovative technique for contrast enhancement of computed tomography images using normalized gamma-corrected contrast-limited adaptive histogram equalization, EURASIP J. Adv. Signal Process. (2015), https://doi.org/10.1186/s13634-015-0214-1.
[32] I.K. Maitra, S. Nag, S.K. Bandyopadhyay, Technique for preprocessing of digital mammogram, Comput. Methods Programs Biomed. 107 (2012) 175–188, https://doi.org/10.1016/j.cmpb.2011.05.007.
[33] G.M. Daiyan, M.A. Mottalib, M.M. Rahman, High performance decision based median filter for salt and pepper noise removal in images, 2012 15th International Conference on Computer and Information Technology (ICCIT), 2012, https://doi.org/10.1109/iccitechn.2012.6509707.
[34] E.R. Dougherty, R.A. Lotufo, Hands-on Morphological Image Processing, SPIE Press. (2003). < https://doi.org/10.1117/3.501104 > .
[35] H. Hassanpour, N. Samadiani, S.M. Salehi, Using morphological transforms to enhance the contrast of medical images, Egyptian J. Radiol. Nucl. Med. 46 (2015) 481–489, https://doi.org/10.1016/j.ejrnm.2015.01.004.
[36] S.S. Shapiro, M.B. Wilk, An analysis of variance test for normality (complete samples), Biometrika 52 (1965) 591–611.
[37] Y. Ozaki, Two-dimensional near-infrared correlation spectroscopy, near-infrared, Spectroscopy (1997) 163–178, https://doi.org/10.1002/9783527612666.ch08.